

Transient penetration of a viscoelastic fluid in a narrow capillary channel

Udugama R. Sumanasekara¹, Martin N. Azese¹ and
Sukalyan Bhattacharya^{1,†}

¹Department of Mechanical Engineering, Texas Tech University, Lubbock, TX 79409, USA

(Received 6 April 2016; revised 5 April 2017; accepted 7 August 2017;
first published online 3 October 2017)

This article describes an unexplored transport phenomenon where a mildly viscoelastic medium encroaches a narrow capillary channel under the action of surface-tension force. The ultimate goal of the study is to provide the penetration length and the intrusion rate of the liquid as functions of time. The resulting analysis would be instrumental in building an inexpensive and convenient rheometric device which can measure the temporal scale for viscoelastic relaxation from the stored data of the aforementioned quantities. The key step in the formulation is a transient eigenfunction expansion of the instantaneous velocity profile. The time-dependent amplitude of the expansion as well as the intruded length are governed by a system of integro-differential relations which are derived by exploiting the mass and momentum conservation principles. The obtained integro-differential equations are simultaneously solved by using a fourth-order Runge–Kutta method assuming a start-up problem from rest. The resulting numerical solution properly represents the predominantly one-dimensional flow which gradually slows down after an initial acceleration and subsequent oscillation. The computational findings are independently verified by two separate perturbation theories. The first of these is based on a Weissenberg number expansion revealing the departure in the unsteady imbibition due to small but finite viscoelasticity. In contrast, the second one explains the long-time behaviour of the system by analytically predicting the decay features of the dynamics. These asymptotic results unequivocally corroborate the simulation inferring the accuracy of the numerics as well as the utility of the simplified mathematical models.

Key words: capillary flows, non-Newtonian flows, viscoelasticity

1. Introduction

The time-dependent imbibition of a purely viscous liquid inside a narrow conduit due to capillary action is a century-old topic in fluid mechanics (Washburn 1921; Szekely, Neumann & Chuang 1970; Chebbi 2007). Such a phenomenon plays a crucial role in natural processes like ground water percolation (Marmur & Cohen 1997) and transport through xylem ducts in plants (Zhmud, Tiberg & Hallstensson 2000). Similarly, surface-tension-driven flow penetration is also important in industrial

† Email address for correspondence: s.bhattacharya@ttu.edu

methods like micro-extrusion (Mitsoulis & Heng 1987) and lithography (Ichikawa, Hosokawa & Maeda 2004). Surprisingly, past studies (Khuzhayorov, Auriault & Royer 2000; Fan, Tanner & Phan-Tien 2001; Bazilevsky *et al.* 2003; Arada, Pires & Sequeira 2005; Mora & Manna 2010) in the related fields have not attempted to formulate a rigorous mathematical theory applicable to an intruding viscoelastic medium instead of a purely viscous one. This article analyses the aforementioned unexplored problem from a theoretical perspective where the penetrated length and intrusion rate of a mildly viscoelastic fluid are calculated as temporal functions.

The existing theories for capillary-driven penetration dynamics of a purely viscous liquid are inherently ill equipped for generalization to systems with viscoelasticity. The reason behind such inability is a crucial assumption taken for granted in earlier studies. According to these approximate formulations (Waghmare & Mitra 2010b; Das, Waghmare & Mitra 2012), an integral approach is applied to describe the rate of intrusion by equating the total force acting on the domain to the rate of change of total momentum. However, while doing so, the viscous resistance on the flow is assumed to be same as the one corresponding to an instantaneous steady condition. This quasi-steady consideration can only be true for slow variation in time, because velocity profile would, otherwise, deviate substantially from its steady version (Bhattacharya & Gurung 2010; Azese 2011). Thus, the resulting analysis would only be valid for problems where the temporal acceleration is much weaker than the viscous dissipation. For mediums governed by linear viscoelastic relations, the modification in the transport process due to rheological properties is typically revealed under highly transient situation. This is why the well-known integral treatments cannot be effectively extended for interesting case studies involving viscoelastic fluid.

In our recent analysis, we have presented a new mathematical procedure that can accurately describe the penetration dynamics of a purely viscous fluid even in the presence of strong transient variations (Bhattacharya, Azese & Singha 2016). The developed theory computes the flow field in terms of an eigenfunction expansion with unknown time-dependent amplitudes. These amplitudes, along with the unsteady encroached length, are calculated from a system of ordinary differential equations which are derived from mass and momentum conservation principles.

The eigen expansion technique is perfectly suited for analysing unsteady intrusion of liquids governed by a linear viscoelasticity relation. In such a case, the system of governing equations would become integro-differential in nature where the rheological property is represented by a temporal integral. In this paper, a fourth-order Runge–Kutta scheme is used to solve these new equations for computation of the unsteady penetration length assuming a start-up problem from rest.

The described generalization can lead to an inexpensive and convenient rheometric device. It is well known that any transiency in a medium reveals its rheology (Groisman, Enzelberger & Quake 2003; Kang & Lee 2013; Koser & Pan 2013; Zilz *et al.* 2014). Accordingly, the proposed rheometer would first record the penetrated length of the fluid as function of time by using any optical device and a data storing equipment. Then, the stored variation can be utilized to predict properties related to viscoelastic relaxation of the intruding liquid by comparing the experimental observation with theoretical expectation for known rheology in an iterative algorithm. For example, if the measurement is accurate enough, the length versus time plot can provide the frequency-dependent real and imaginary parts of complex viscosity, leading to the evaluation of viscoelastic coefficients like G' and G'' often referred to as the storage and loss moduli, respectively.

Apart from rheometry, the developed theory can also be relevant in estimating the absorption rate of complex fluids in a porous medium. Such an application

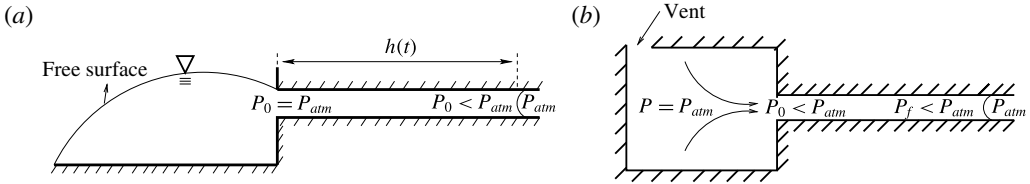


FIGURE 1. (a) The system considered in our analysis where a capillary channel transports fluid from a drop with a free surface due to the surface tension effect. (b) Earlier works have considered a slightly different problem where the supplying fluid body is confined in an infinite chamber requiring a mathematical model for entry loss before the entrance.

can contribute in the removal of oil spillage as well as in the development of new absorbing materials.

This article is organized in the following way. In §2, we outline the generalized mathematical formulation leading to the system of integro-differential relations involving the transient amplitudes and unsteady intrusion length. In §3, the coupled equations are solved simultaneously with a fourth-order Runge–Kutta scheme to compute the penetration and its rate as functions of time. Section 4 verifies the simulation results by a novel Weissenberg number expansion which provides further insight in the short-time dynamics of the system. In contrast, §5 corroborates the long-time dynamics revealed in the computation by introducing another different perturbation theory. Finally, the article is summarized, and conclusions are drawn in §6.

2. Transient eigenfunction expansion for viscoelastic flow

In this section, we present the details of our mathematical analysis for the unsteady intrusion dynamics of a linearly viscoelastic liquid driven by surface tension into a narrow capillary channel. Accordingly, the flow equations are non-dimensionalized, and the instantaneous velocity profile is expanded in terms of appropriate eigenfunctions. Ultimately, our derivation yields a system of integro-differential equations involving the transient amplitudes of the eigen expansion and the time-dependent penetration length.

2.1. The flow system

In our analysis, we consider a horizontal capillary channel of cross-sectional area A and perimeter s . It is initially prefilled with a liquid column of length h_0 and in contact with a drop of the same substance. The empty part of the conduit is totally unwetted as long as it is not being occupied by the intruding fluid. The cross-sectional dimension of the tube is assumed to be much smaller than the size of the drop so that it can be approximated as an infinite reservoir with a free surface. The contact point between the drop and the channel is very near to the free surface so that the flow inside the vessel is solely driven by capillary action without any gravitational influence. The system is schematically described in figure 1. It also shows side by side the arrangement considered in earlier works where pressure at the entry point has to be evaluated by modelling the outside flow. Such a calculation is not needed in our case as the atmospheric condition prevails at the entrance of our considered system.

The conduit is assumed to be prefilled by a liquid column of initial length h_0 before the start of the dynamics. We anticipate the need for such partial filling

for accurate rheological measurements. This is because the discrepancy between the theoretical prediction and the experimental data can be unnecessarily high due to entry effects if the penetrated distance is of the order of the cross-sectional dimensions. In the rheometric set-up, h_0 can be introduced by either using a retractable barrier or dissolvable obstacle in the path of the fluid. As a result, the motion in the system vanishes for some time after reaching a distance, and resumes from a stationary condition after removal of the blockage. Accordingly, the additional parameter h_0 in the analysis will provide us with the mathematical flexibility to accommodate future experimental necessity. If this feature is not needed, h_0 can simply be taken as 0.

The encroaching medium is a complex fluid whose dynamics is governed by a linear viscoelastic equation. As a result, the instantaneous stress σ in the liquid domain is dependent on a weighted history of the velocity field v so that

$$\sigma = \mu_0[\nabla(\hat{L}_t v) + \{\nabla(\hat{L}_t v)\}^T]. \tag{2.1}$$

Here, superscript T represents transpose, μ_0 is the steady-state viscosity and \hat{L}_t is an integral operator in time t and τ

$$\hat{L}_t v|_t = \frac{1}{\tau_v} \int_{-\infty}^t M\left(\frac{t-\tau}{\tau_v}\right) v(\tau) d\tau. \tag{2.2}$$

The dimensionless weight function M manifests the viscoelastic effect by including the cumulative influence of past strain rates on the instantaneous stress at a point in the medium (Rousse Jr 1953). Different mildly viscoelastic liquids can be characterized by the memory function M . For example, a Maxwell fluid is defined by an exponential M . For purely viscous case, M becomes a Dirac delta function, so that stress depends only on the strain rate at that instant and \hat{L}_t transforms to an identity operator. Fourier transform of M yields the complex viscosity normalized by μ_0 . Consequently, it would be also possible to evaluate the frequency-dependent viscoelastic coefficients G' and G'' of the medium by relating them to the real and imaginary parts of the Fourier transform of M .

The definition of steady-state viscosity μ_0 implies the zeroth moment of the memory function M is unity. The convolution in (2.2) explicitly involves the effective time scale τ_v for viscoelastic relaxation. It can be uniquely obtained by ensuring the first moment of M to be unity. In that case, even if the medium involves multiple scales for relaxation, their weighted average would be expressed by τ_v . In other words, the definitions of μ_0 and τ_v impose two constraints on the functional distribution of the non-dimensional weight function M by specifying two of its moments

$$\int_0^\infty M(\zeta) d\zeta = 1 \quad \text{and} \quad \int_0^\infty \zeta M(\zeta) d\zeta = 1. \tag{2.3a,b}$$

Properties of any mildly viscoelastic liquid can be represented by μ_0 , τ_v and $M(\zeta)$ with ζ being the normalized time interval. Even if multiple time scales of relaxation are present, these can be described by combining τ_v and $M(\zeta)$, where the latter would reveal non-trivial non-monotonic variations.

The fluid domain mainly contains unidirectional but transient flow as long as $h_0 \gg s$. So apart from the two ends of the liquid column, the dynamics is represented by the velocity component v_z along the direction z of the channel length. Accordingly, the

system is governed by the following momentum equation involving v_z and pressure p

$$\rho \frac{\partial v_z}{\partial t} = \mu_0 \nabla_{\parallel}^2 \hat{L}_t v_z - \frac{\partial p}{\partial z}, \quad (2.4)$$

where ρ is the density of the encroaching medium and ∇_{\parallel} is the gradient in cross-sectional plane. When (2.4) is combined with the integral mass balance equation involving average over cross-sectional area A

$$\frac{dh}{dt} = \frac{1}{A} \int v_z dA, \quad (2.5)$$

the penetrated length h can be evaluated as function of t .

2.2. Scaling and non-dimensionalization

We solve (2.4) and (2.5) in dimensionless form to provide a concise and general description of the transport phenomenon. This requires identification of proper scales for the variables relevant in the dynamics of the system.

The scales for the cross-sectional coordinates and pressure field are readily available from the geometric and parametric properties. The former is defined as b_c , and identified as the area-to-perimeter ratio. The latter, denoted P_s , is determined by equating the average forces due to pressure and capillary action. This means that P_s is the cross-sectional mean of the Laplace pressure near the propagating interface. Thus, we conclude:

$$b_c = \frac{A}{s} \quad \text{and} \quad P_s = \frac{\gamma s}{A}. \quad (2.6a,b)$$

Here, the constant γ corresponds to the net capillary force along z if multiplied by the cross-sectional projection of the perimeter. It is given by the difference between surface-tension coefficients γ_{sa} and γ_{sl} for solid–air and solid–liquid interfaces, respectively. Equivalently, due to equilibrium of the contact line, γ is the same as the product of the liquid–air interfacial tension γ_{la} and the cosine of the contact angle θ . This means that

$$\gamma = \gamma_{sa} - \gamma_{sl} = \gamma_{la} \cos \theta. \quad (2.7)$$

For low capillary number, γ does not vary, as the propagating front does not change its shape considerably during the transport process keeping the contact angle θ fixed.

The remaining scales correspond to the penetration length, the phenomenal duration and the velocity field. These are not only dependent on geometric and material parameters but also dictated by the period of the relevant transport process. Kinematic consideration concludes the velocity scale v_s to be the ratio of characteristic penetration h_s and time t_s . However, we need two more constraints to ultimately determine v_s , h_s , t_s . At this point, we recall that for rheometry, one has to resolve the timeframe in which transient effects are comparable to the dissipative influence of viscous friction. As a result, the characteristic values for both should be equated to the same for the pressure term induced by the capillary action. So one can derive the following conditions

$$\frac{h_s}{t_s v_s} = 1, \quad \frac{t_s \mu_0}{\rho b_c^2} = 1, \quad \frac{\gamma t_s}{\rho b_c h_s v_s} = 1. \quad (2.8a-c)$$

From these it is inferred that

$$t_s = \rho b_c^2 / \mu_0, \quad h_s = b_c \sqrt{\rho \gamma b_c / \mu_0^2}, \quad v_s = \sqrt{\gamma / (\rho b_c)}. \tag{2.9a-c}$$

This implies that t_s is defined as the relevant period for viscous dissipation in (2.9). The infiltration and its rate are characterized by h_s and v_s accordingly. For rheometric purposes, t_s and τ_v should be comparable. Under such conditions, however, the integral approximation calculating resistance from the steady-state profile would not be accurate enough.

The scales defined in (2.6) and (2.9) are used to normalize all quantities in (2.4) and (2.5). As a result, the non-dimensional governing relations become

$$\frac{\partial \bar{v}_z}{\partial \bar{t}} = \bar{\nabla}_{\parallel}^2 \hat{L}_t \bar{v}_z - \frac{\partial \bar{p}}{\partial \bar{z}} \quad \text{and} \quad \frac{d\bar{h}}{d\bar{t}} = \frac{1}{A} \int \bar{v}_z dA, \tag{2.10a,b}$$

where $\bar{v}_z = v_z / v_s$, $\bar{t} = t / t_s$, $\bar{p} = p / P_s$, $\bar{h} = h / h_s$ are all dimensionless and $\bar{\nabla}_{\parallel}$ is the cross-sectional gradient normalized by b_c . The corresponding dimensionless interpretation of the operator \hat{L}_t in (2.2) redefines it as

$$\hat{L}_t \bar{v}_z = \frac{1}{Wi} \int_{-\infty}^{\bar{t}} M \left(\frac{\bar{t} - \bar{\tau}}{Wi} \right) \bar{v}_z(\bar{\tau}) d\bar{\tau}. \tag{2.11}$$

Here, Wi is the Weissenberg number

$$Wi = \frac{\tau_v \mu_0}{\rho b_c^2}, \tag{2.12}$$

which is a system-defining non-dimensional parameter denoting the ratio of the time scales for viscoelastic relaxation and the transient transport process.

2.3. Estimation of the pressure gradient

The capillary effect on the flow is manifested by suction at the propagating front. This creates a driving pressure gradient across the region of unidirectional streamlines

$$\frac{\partial \bar{p}}{\partial \bar{z}} = \frac{\Delta \bar{p}}{\bar{h}}, \tag{2.13}$$

where the dimensionless suction pressure between two ends of the domain is $\Delta \bar{p}$. We provide a proper model for $\Delta \bar{p}$, and solve (2.10) to describe the transport process.

In past studies (Stange, Dreyer & Rath 2003; Waghmare & Mitra 2010a; Das *et al.* 2012) on this topic, $\Delta \bar{p}$ is related to two separate pressure drops. The first of these appears outside the inlet of the channel where the pressure has to be slightly less than the ambient far away from the entry point to sustain a converging flow towards the conduit. Our problem, however, is fundamentally different from the systems considered in the earlier works where the capillary vessel sucks from an infinite body of fluid without exposure to the atmosphere in close proximity. In contrast, we have a free-surface reservoir in the form of an infinite drop with its atmospheric interface situated very near to the entrance. As mentioned before, this distinction is well represented in the two diagrams in figure 1. Thus, in the present problem, there is no difference in elevation between the inlet and the atmosphere. Moreover, the

large size of the drop ensures negligible Laplace pressure in its interior. So one can safely assume an ambient condition at the entrance of the channel. As a result, we can find $\Delta\bar{p}$ by only taking into account the second contribution in $\Delta\bar{p}$ coming from the region attached to the propagating front.

The region near the front contains axially varying flow with three-dimensional structure transforming the unidirectional profile into a flow near a propagating front. Thus, the three-dimensional unsteady Navier–Stokes equation should govern the hydrodynamic fields here. Still, the scales for time, cross-sectional dimension, velocity and pressure must be identical between the two adjacent regions with one-dimensional and three-dimensional streamlines. The only scale which changes between these two subdomains is the axial length scale, which is b_c for the latter instead of h_s , defined as the characteristic penetrated distance in § 2.2. When this change is included in the dimensional analysis, it makes the pressure gradient and the convective acceleration predominant over temporal and viscous terms. Consequently, one finds a new dimensionless momentum equation for velocity $\bar{\mathbf{v}}$

$$\delta \frac{\partial \bar{\mathbf{v}}}{\partial \bar{t}} + \bar{\mathbf{v}} \cdot \nabla \bar{\mathbf{v}} = -\bar{\nabla} \bar{p} + \delta \bar{\nabla}^2 \hat{L}_t \bar{\mathbf{v}}. \quad (2.14)$$

The constant non-dimensional parameter δ represents the effective capillary number which is the ratio of the characteristic viscous and surface-tension forces relevant to the system

$$\delta = \sqrt{\mu_0^2 / (\rho \gamma b_c)} = b_c / h_s. \quad (2.15)$$

If b_c is much greater than 100 nanometres, δ is a very small quantity for a wide range of fluids. We are typically interested in cross-sectional dimensions of a few millimetres. Then, the value of δ becomes less than 10^{-3} . Hence, we can safely identify δ to be a very small quantity. Such a fact does not affect the transient nature of the unidirectional flow, as the pressure gradient there becomes comparable to the viscous and temporal terms due to the rescaling of the axial scale from b_c to h_s . This, however, simplifies the analysis near the front in two ways. Firstly, it makes the viscous resistance at the boundary layer attached to any interface negligible, especially in the calculation of the leading-order pressure field. Secondly, we can assume the shape of the propagating front to be fixed, as a small value of δ implies a small capillary number and a much stronger capillary force compared to the viscous stress. Consequently, for leading-order analysis in δ , $\Delta\bar{p}$ near the front should be obtained from a steady inviscid flow equation near an undeformed free surface. This is why all the past studies (Stange *et al.* 2003; Waghmare & Mitra 2010a; Das *et al.* 2012) have correctly obtained the pressure drop across the front region by using conservation of linear momentum without considering any boundary layer dissipation or interfacial deformation. We import their conclusion into our present analysis.

Accordingly, we note that the cross-sectional average $\Delta\bar{p}_f$ of the non-dimensional Laplace pressure at the front must be -1 due to the normalizing scale. This nominal value should be modified according to linear momentum conservation at the subdomain attached to the front to find the pressure $\Delta\bar{p}$ at the transition point between the unidirectional and three-dimensional flow. The difference between $\Delta\bar{p}$ and $\Delta\bar{p}_f$ should be equated to a change in linear momentum flux across the region. When we substitute $\Delta\bar{p}_f$ as -1 in this integral momentum relation, we find the well-known expression (Waghmare & Mitra 2010a)

$$\Delta\bar{p} = \left(\int \bar{v}_z d\bar{A} \right)^2 - \int \bar{v}_z^2 d\bar{A} - 1, \quad (2.16)$$

where $d\bar{A} = dA/A$. When the expression for $\Delta\bar{p}$ is combined with (2.10) and (2.13), the final form of the governing relation can be derived

$$\frac{\partial \bar{v}_z}{\partial \bar{t}} = \nabla_{\parallel}^2 \hat{L}_t \bar{v}_z + \frac{1 + \int \bar{v}_z^2 d\bar{A} - \left(\int \bar{v}_z d\bar{A} \right)^2}{\bar{h}} \quad \text{and} \quad \frac{d\bar{h}}{d\bar{t}} = \int \bar{v}_z d\bar{A}, \quad (2.17a,b)$$

which has to be solved to compute the flow field, the transport rate and the time-dependent penetration length.

2.4. Eigenfunction expansion

To obtain the flow solution, we consider a transient eigenfunction expansion of the velocity \bar{v}_z , so that the unsteady flow is expressed in a separable form:

$$\bar{v}_z = \sum \alpha_i(\bar{t}) u_i(\bar{\mathbf{r}}_{\parallel}). \quad (2.18)$$

Here, time-dependent amplitudes are α_i , whereas time-invariant eigenfunctions u_i only vary with $\bar{\mathbf{r}}_{\parallel}$ which is the cross-sectional coordinates normalized by b_c . A Helmholtz equation corresponding to the following eigen value equation defines u_i

$$\nabla_{\parallel}^2 u_i = -\beta_i^2 u_i, \quad (2.19)$$

where $-\beta_i^2$ are the allowable eigen values for which u_i can satisfy no-slip boundary conditions at the periphery of the vessel. Sturm–Liouville theorem confirms that the eigenfunctions u_i for any arbitrary geometry should be orthogonal to each other. We normalize u_i in such a way that they become orthonormal as well:

$$\int u_i u_j d\bar{A} = \delta_{ij}, \quad (2.20)$$

where δ_{ij} is the Kronecker delta. These functions can be constructed for any cross-section of interest using standard techniques such as the finite volume technique (Patankar 1980).

Ideally, the summation in (2.18) is an infinite one. However, we truncate it at a finite but reasonably high limit so that the solution of \bar{v}_z is properly represented in the spectral space. Then, a complete set of integro-differential equations is derived involving all relevant $\alpha_i(\bar{t})$ as well as $\bar{h}(\bar{t})$ by considering two facts. Firstly, the linear momentum conservation relation in (2.17) is exploited to obtain the number, N , of independent equations for the same number of eigen modes included in the analysis. Secondly, the integral mass conservation also provides a single relation involving $\bar{h}(\bar{t})$ and all $\alpha_i(\bar{t})$. This means that there are $(N + 1)$ unknowns including $\alpha_1, \alpha_2, \dots, \alpha_N$ as well as $\bar{h}(\bar{t})$. These have to be evaluated by simultaneously solving the $(N + 1)$ coupled equations.

In our derivation, we first derive the expression of $\Delta\bar{p}$ in terms of eigen amplitudes $\alpha_i(\bar{t})$ by applying Parseval theorem in (2.16)

$$\Delta\bar{p} = \left(\sum \eta_i \alpha_i \right)^2 - \sum \alpha_i^2 - 1, \quad (2.21)$$

where η_i is the cross-sectional integral of u_i

$$\eta_i = \int u_i \, d\bar{A}. \tag{2.22}$$

Then, \bar{v}_z is replaced in the linear momentum conservation relation of (2.17) with the expansion (2.18). The resulting equality is multiplied by the i th eigenfunction u_i , and integrated over the cross-section. Then, equations (2.19)–(2.22) are used to obtain the following:

$$\frac{d\alpha_i}{d\bar{t}} = -\beta_i^2 \hat{L}_i \alpha_i + \eta_i \frac{1 + \sum \alpha_j^2 - (\sum \eta_j \alpha_j)^2}{\bar{h}} \tag{2.23}$$

for $i = 1, 2, \dots, N$. The remaining equation is obtained from mass conservation so that the rate of penetration can be expressed in terms of α_i and η_i

$$\frac{d\bar{h}}{d\bar{t}} = \sum_{i=1}^N \eta_i \alpha_i(\bar{t}). \tag{2.24}$$

We solve (2.23) and (2.24) simultaneously to find $\bar{h}(\bar{t})$ and relevant $\alpha_i(\bar{t})$.

3. Unsteady intruded length and its rate for rectangular channels

In this section, we solve (2.23) and (2.24) simultaneously to compute $\alpha_i(\bar{t})$ and $\bar{h}(\bar{t})$ considering the capillary channel to be rectangular in shape. As an outcome, the intrusion rate and the penetration length are evaluated as functions of time. The results are presented for different prefilled length h_0 and Weissenberg number Wi . Considering practical rheometric applications, we choose h_0 to be of the order of h_s and Wi to be less than 1. Also, we take into account two aspect ratios for the rectangular conduit which is assumed to be either a square or a slit pore. Finally, we briefly outline the algorithm to extract rheological properties from the observed transiency in penetration dynamics.

3.1. Details of the numerical solution scheme

The computation requires determination of the geometric parameters representing the shape of the conduit. These are the eigenfunctions u_i , eigen values β_i^2 and cross-sectional integrals η_i . However, we recognize that we need two eigen parameters associated with the two-dimensional feature of a rectangular cross-section. Accordingly, we replace the subscript i by two indices n and m . Thus, from now on, u_i , β_i and η_i will be referred to as u_{nm} , β_{nm} and η_{nm} , respectively. For a rectangular tube, these quantities are

$$u_{nm} = 2 \cos\left(\frac{2n+1}{2} \pi \frac{\bar{x}}{\bar{L}_x}\right) \cos\left(\frac{2m+1}{2} \pi \frac{\bar{y}}{\bar{L}_y}\right), \tag{3.1}$$

$$\beta_{nm}^2 = \frac{\pi^2}{4} \left[\frac{(2n+1)^2}{\bar{L}_x^2} + \frac{(2m+1)^2}{\bar{L}_y^2} \right] = \frac{\pi^2}{4(1+\lambda)^2} [\lambda^2(2n+1)^2 + (2m+1)^2], \tag{3.2}$$

and

$$\eta_{nm} = \frac{8}{\pi^2} \frac{(-1)^{n+m}}{(2n+1)(2m+1)}. \tag{3.3}$$

Here, \bar{x} and \bar{y} are the x and y coordinates normalized by $b_c = A/s$, whereas \bar{L}_x and \bar{L}_y are the non-dimensional lengths of the sides along the x and y axes. The aspect ratio of the cross-section is defined by λ which is the ratio of \bar{L}_x and \bar{L}_y . Although ideally an infinite number of eigenfunctions should be considered, we take the maximum value for both m and n to be 40. This ensures less than 0.01 % relative error due to the spectral convergence.

Subsequent computation considers the flow to be driven by the capillary action from an initially static condition with an initial prefilled length h_0 . So the simulation essentially solves a start-up problem where the initial conditions are taken as $\bar{h}(0) = h_0 = h_0/h_s$ and $\alpha_{nm}(0) = 0$. Then, a fourth-order Runge–Kutta scheme is used to simultaneously compute $\bar{h}(\bar{t})$ and $\alpha_{nm}(\bar{t})$ from (2.23) and (2.24).

In each time step, we apply a Simpson technique to calculate the integral in the operator \hat{L}_t defined by (2.2) representing the effect of viscoelasticity. In this integral, the lower limit is replaced by 0 in place of $-\infty$, as there has been no motion before the initial time. Then stored past values of α_{nm} are multiplied with the memory function M , and the product is numerically integrated to determine the viscoelastic stress in (2.23). The fluid is considered to be a Maxwell fluid so that M is exponential in nature

$$M(\zeta) = e^{-\zeta}. \tag{3.4}$$

It is to be noted that (3.4) satisfies both constraints for M as shown in (2.3).

3.2. Temporal variation in penetration dynamics

The outlined solution scheme finds the rate of imbibition of the viscoelastic liquid by using the computed values of α_{nm} at each time step in (2.24). The intrusion rate is presented as a temporal function in figure 2. The result is obtained for both square channels and slit pores. Moreover, the simulation considers two different prefilled lengths for each geometry, as well as two values of the Weissenberg number to illustrate the impact of viscoelasticity. For mildly viscoelastic fluids like dilute polymeric solutions, a typical Weissenberg number should be less than 1. If the Weissenberg number becomes more than 1, the medium might not be governed by a linear viscoelastic law. This is the rationale behind choosing the specific Wi values for the plots shown in figure 2. For proper comparison, the quantities are also calculated for a purely viscous fluid as a base case.

In figure 2, higher values of the Weissenberg number Wi imply a stronger viscoelastic effect causing significant departure in the short-time dynamics from the behaviour of a purely viscous liquid. Initially, the resistive stress in a viscoelastic fluid is less than the same for a viscous medium. So, the transport rate for the former is higher than the latter in the initial phase. At a later time, however, the difference is reversed, as the flow is pushed back in overcompensation after the relaxation of the memory effect. Such a reversal is a common feature in systems with viscoelasticity (Felderhof 2009). Further explanation for the temporal oscillation is provided in § 4 where the Weissenberg number perturbation is described.

We expect the intrusion rate to decrease with the prefilled length h_0 . This is because a higher value of h_0 means a higher resistance to the flow. Such behaviour is evident in figure 2. It is to be noted, however, that h_0 does not affect the temporal period over which the relative departure between the viscoelastic and the purely viscous systems occurs.

Curves for different Wi eventually approach the one for a purely viscous fluid under the long-time limit. The leading-order decay characteristic is actually

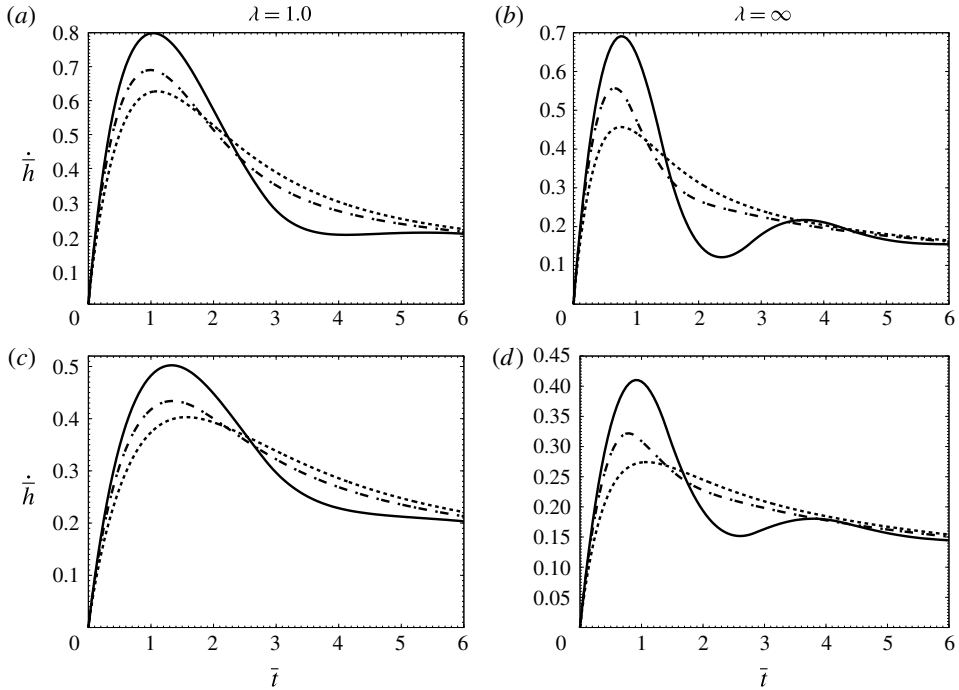


FIGURE 2. Dimensionless encroachment rates versus normalized time for a square channel (*a,c*) and slit pore (*b,d*) with initial prefilled length 0.5 (*a,b*) and 1.0 (*c,d*). The Weissenberg number Wi is considered to be 0.5 (solid lines) and 0.2 (dash-dot line), whereas the dotted lines represent the curves for a purely viscous fluid.

independent of Wi . However, the next-order asymptotic decrease does depend on Wi . Details of this feature are described in our subsequent perturbation analysis in § 5.

We also note that the flow rate is higher in a square channel compared with a slit pore. This is an expected behaviour, as the former is more conducive than the latter as long as the hydraulic radius given by $2b_c$ is the same for both.

The computation also provides the penetrated length at each time step. We plot this as a temporal function in figure 3 for all the parametric values considered in figure 2.

The plots reveal two regimes of temporal variation. In the initial time, the penetration increases linearly. However, under the long-time limit, it shows Washburn's prediction $\bar{h} \sim \sqrt{\bar{t}}$. These results are corroborated by recent experiments (Quere 1997; Das *et al.* 2012).

From figure 3, one can conclude that the penetrated length h is always larger in systems with higher Wi at any temporal point. Although the intrusion rate is overcompensated after the initial larger value in a viscoelastic fluid, the compensation is not strong enough to reverse the difference in h . Also, $h(t)$ for fixed Wi is higher for a larger prefilled length as well as for a square channel compared to a slit pore.

3.3. Postprocessing algorithm for rheometry

In the actual rheometric experiments, the rheological properties defined by the memory function M have to be detected from the observed transiency in the penetration rate. This is the reverse calculation of what is presented in § 3.2, where time-dependent

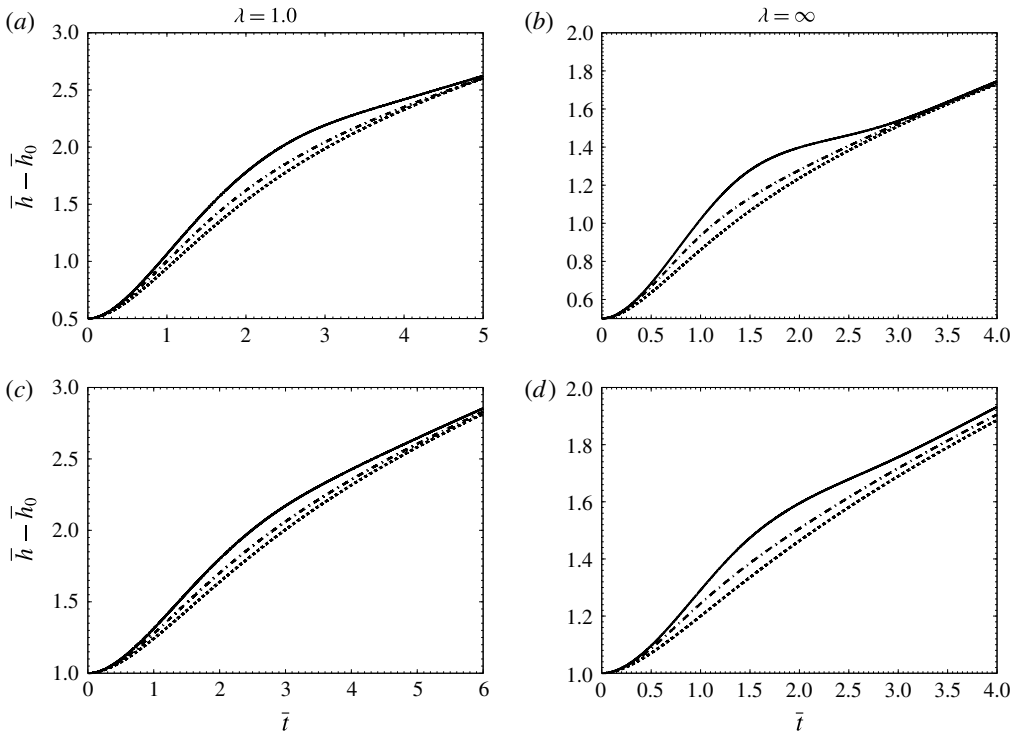


FIGURE 3. Dimensionless encroachment length versus normalized time for a square channel (a,c) and slit pore (b,d) with initial prefilled length 0.5 (a,b) and 1.0 (c,d). Weissenberg number Wi is considered to be 0.5 (solid lines) and 0.2 (dash-dot line), the dotted lines represent curves for a purely viscous fluid.

behaviour is computed for given M . Thus, an effective measurement technique requires an inversion algorithm.

The first step for this reverse analysis is to consider the temporal Fourier transform of (2.4). The resulting relation is, then, convoluted with the spatial eigenfunctions u_{nm} . As a result, after rearrangement, one finds

$$v_s \hat{\alpha}_{nm} = \frac{\eta_{nm} \hat{f}(\omega)}{i\rho\omega + \mu_0 \hat{\mu} \beta_{nm}^2 / b_c^2}. \tag{3.5}$$

Here, ω is the Fourier frequency, whereas the transformations of the amplitudes, memory function and force density are given as

$$\hat{\alpha}_{nm} = \int e^{-i\omega t} \alpha_{nm}(t) dt, \quad \hat{\mu} = \int e^{-i\omega t} M(t) dt, \quad \hat{f} = - \int e^{-i\omega t} \frac{\partial p}{\partial z} dt. \tag{3.6a-c}$$

At this point, we consider (2.24) in dimensional form and conclude the Fourier transform \hat{j} for penetration rate to be

$$\hat{j}(\omega) = \int e^{-i\omega t} \dot{h} dt = v_s \sum \eta_{nm} \hat{\alpha}_{nm}. \tag{3.7}$$

When (3.5) and (3.7) are combined, the inversion relation is derived

$$\hat{j}(\omega) = \sum_{nm} \frac{\eta_{nm}^2 \hat{f}(\omega)}{i\rho\omega + \mu_0 \hat{\mu}(\omega) \beta_{nm}^2 / b_c^2}. \quad (3.8)$$

If \hat{j} and \hat{f} are known, the only unknowns remaining in (3.8) are the nominal viscosity for steady state μ_0 and the normalized frequency-dependent complex coefficient $\hat{\mu}$. The postprocessing algorithm exploits (3.8) to determine these rheological properties.

From the recorded experimental data, \hat{j} can be obtained directly from the Fourier transform of the dimensional version of the plots presented in figure 2. In contrast, \hat{f} has to be determined iteratively due to the presence of the subdominant but non-zero convective terms in (2.16). Still, in the first approximation, one can consider \hat{f} to be a simple Fourier transform of inverse of the penetration length h representing the predominant capillary effect. Then one can solve (3.8) for different ω to find μ_0 and $\hat{\mu}(\omega)$. For $\omega = 0$, normalized $\hat{\mu}$ is 1 by definition. Hence, for such a steady-state ω value, equation (3.8) yields the actual value for μ_0 . Once this is evaluated, $\hat{\mu}$ can be calculated for non-zero ω . When the complete description of the rheology is available, one can repeat the flow analysis presented earlier to compute the hydrodynamic fields. As a result, the small convective contribution can be included in a more accurate \hat{f} . A subsequent solution of (3.8) would, next, render new values for the rheological properties. In this way, an iterative scheme can be devised to improve \hat{f} and the frequency-dependent viscosity in successive iterations until the results converge. The smallness of the convection term ensures the fast convergence of the proposed algorithm.

If μ_0 and $\hat{\mu}(\omega)$ are determined, the frequency-dependent complex viscosity would be known for a mildly viscoelastic medium. Then, the memory function M can be constructed from the Fourier transform of $\hat{\mu}$ in the spectral domain and the viscoelastic time scale can be detected using the first moment normalization in (2.3). Also, the viscoelastic coefficients G' and G'' are related to $\mu_0 \hat{\mu}(\omega)$ by known simple expressions. Thus, the outlined procedure can determine the desired viscoelastic coefficients from easily acquired experimental data. Such technology has the potential to provide an accurate and cost effective means for rheometric measurement.

4. Perturbation analysis by Weissenberg number expansion

The effect of the viscoelasticity on the short-time dynamics can be quantified by the departure from the base case for the purely viscous liquid. For a mildly viscoelastic medium with a Weissenberg number $Wi < 1$, temporal variation in such difference between viscous and viscoelastic systems can be mathematically described by using a perturbation analysis. This theory can provide precise explanation to understand the transport phenomenon better.

The analysis is based on the perturbation of Wi , which is considered as a small parameter. It shows how the leading-order difference between a viscous and viscoelastic medium can be expressed in terms of expansion terms in Wi . Moreover, the perturbative relations are simplified to an approximate formulation where the effect of viscoelasticity can be described by a single second-order linear ordinary differential equation. The time-dependent spring, damping and forcing terms in the reduced model help to understand the temporal oscillations in the system of interest seen in figure 2.

We compare the computed departure between a viscous and viscoelastic medium with the exact perturbation theory and the approximate reduced description. All three sets of results match with each other with the expected accuracy. As a result, our numerical results can be independently verified. Moreover, the simplified but approximate mathematical model can be utilized as a useful tool which provides both faster quantitative calculation and further insight into the transient dynamics.

4.1. Taylor series expansion of the viscoelastic term

The first step in the perturbation analysis is to represent the following viscoelasticity term in a power series of the Weissenberg number:

$$\hat{L}_t \alpha_i |_{\bar{t}} = \frac{1}{Wi} \int_{-\infty}^{\bar{t}} M \left(\frac{\bar{t} - \bar{\tau}}{Wi} \right) \alpha_i(\bar{\tau}) d\bar{\tau}. \tag{4.1}$$

Here M is taken as a considerably localized distribution for small Weissenberg number, which implies $t_s \gg \tau_v$. As a result, we can disregard any difference in the viscoelastic dynamics caused by the initial condition of the system.

For the Weissenberg number expansion, we consider the following change in variable

$$(\bar{t} - \bar{\tau})/Wi = \zeta \implies \bar{\tau} = \bar{t} - Wi\zeta. \tag{4.2}$$

The new temporal variable ζ represents the time relevant to the viscoelastic scale instead of the transport scale. This transforms the viscoelastic integral

$$\hat{L}_t \alpha_i |_{\bar{t}} = \int_0^{\infty} M(\zeta) \alpha_i(\bar{t} - Wi\zeta) d\zeta, \tag{4.3}$$

which is an equivalent reinterpretation of the memory effect.

We note that a Taylor series expansion in Wi yields

$$\alpha_i(\bar{t} - Wi\zeta) = \sum_{n=0}^{\infty} \frac{(-Wi\zeta)^n}{n!} \frac{d^n \alpha_i}{d\bar{t}^n}. \tag{4.4}$$

When (4.4) is substituted into (4.3), one finds

$$\hat{L}_t \alpha_i |_{\bar{t}} = \sum_{n=0}^{\infty} (-1)^n Wi^n \frac{M_n}{n!} \left. \frac{d^n \alpha_i}{d\bar{t}^n} \right|_{\bar{t}}, \tag{4.5}$$

where,

$$M_n = \int_0^{\infty} \zeta^n M(\zeta) d\zeta \tag{4.6}$$

is the n th moment of the distribution $M(\zeta)$ with M_0 and M_1 both being 1 as per (2.3).

4.2. Perturbation expansion in the Weissenberg number

The leading-order effect of the viscoelasticity on the dynamics is captured by expanding the dependent variables of (2.23) and (2.24) in power series of Wi

$$\alpha_i = \alpha_i^{(0)} + Wi\alpha_i^{(1)} + \dots, \quad \bar{h} = \bar{h}^{(0)} + Wi\bar{h}^{(1)} + \dots. \tag{4.7a,b}$$

Here, the superscript 0 represents the quantities corresponding to the purely viscous fluid. In contrast, the first-order corrections in these variables due to viscoelasticity are denoted by the superscript 1.

We replace the dependent variables in (2.24) by their respective expansions, and form the mass conservation relation for each order in Wi

$$\frac{d\bar{h}^{(k)}}{d\bar{t}} = \sum_{i=1}^N \eta_i \alpha_i^{(k)}(\bar{t}), \tag{4.8}$$

where k is either 0 or 1. When (2.23) is similarly modified using (4.5)–(4.7) and arranged according to the exponent of Wi , the zeroth-order recovers the momentum equation for the purely viscous flow (Bhattacharya *et al.* 2016)

$$\frac{d\alpha_i^{(0)}}{d\bar{t}} + \beta_i^2 \alpha_i^{(0)} = \frac{\eta_i}{h^{(0)}} \left[1 + \sum [\alpha_j^{(0)}]^2 - \left(\sum \eta_j \alpha_j^{(0)} \right)^2 \right]. \tag{4.9}$$

Also the leading-order correction in momentum conservation due to viscoelastic stress is represented by

$$\frac{d\alpha_i^{(1)}}{d\bar{t}} + \beta_i^2 \left[\alpha_i^{(1)} - \frac{d\alpha_i^{(0)}}{d\bar{t}} \right] = 2\eta_i \frac{\sum \alpha_j^{(0)} \alpha_j^{(1)} - \dot{h}^{(0)} \dot{h}^{(1)}}{h^{(0)}} - \eta_i h^{(1)} \frac{1 + \sum [\alpha_j^{(0)}]^2 - \left(\sum \eta_j \alpha_j^{(0)} \right)^2}{[h^{(0)}]^2}. \tag{4.10}$$

In our earlier paper (Bhattacharya *et al.* 2016), we solve (4.8) and (4.9) to obtain the zeroth-order temporal variations given by $\bar{h}^{(0)}$ and $\alpha_i^{(0)}$. These known functions are used in (4.10) to determine the leading-order corrections $\bar{h}^{(1)}$ and $\alpha_i^{(1)}$.

4.3. Simplified mathematical model

We attempt to describe the corrections $\bar{h}^{(1)}$ and $\alpha_i^{(1)}$ in two ways. Firstly, equations (4.8) and (4.10) are solved exactly by numerical means using the Runge–Kutta method assuming a start-up problem from rest. These precise solutions, however, are not adequate for a complete physical understanding so we also pursue a second approach, where necessary simplifications are assumed so that the results can be justified more intuitively. Also such alternative analysis can verify the simulation independently.

Accordingly, we first simplify (4.10) for $i > 0$ by neglecting the quadratic terms involving the zeroth-order amplitudes $\alpha_j^{(0)}$

$$\frac{d\alpha_i^{(1)}}{d\bar{t}} + \beta_i^2 \alpha_i^{(1)} = \beta_i^2 \frac{d\alpha_i^{(0)}}{d\bar{t}} - \frac{\eta_i h^{(1)}}{[h^{(0)}]^2} + \frac{2\eta_i}{h^{(0)}} \left[\sum \alpha_j^{(0)} \alpha_j^{(1)} - \dot{h}^{(0)} \dot{h}^{(1)} \right]. \tag{4.11}$$

The rationale behind this simplification is derived from our prior study on purely viscous flow where $\alpha_j^{(0)}$ is seen to be much less than unity.

Next, we also observe β_i is much larger than unity for any channel when $i > 0$. This means that $\alpha_i^{(1)}$ for $i > 0$ saturates quickly to its long-time solution due to the fast exponential decay of the contribution from the initial condition. Hence, for $i > 0$, we approximate the long-time solution of (4.11) to be the actual $\alpha_i^{(1)}$

$$\alpha_i^{(1)}(\bar{t}) = (1 - e^{-\beta_i^2 \bar{t}}) \frac{d\alpha_i^{(0)}}{d\bar{t}} - \frac{1}{\beta_i^2} \left[\frac{\eta_i h^{(1)}}{[h^{(0)}]^2} - \frac{2\eta_i}{h^{(0)}} \left\{ \sum \alpha_j^{(0)} \alpha_j^{(1)} - \dot{h}^{(0)} \dot{h}^{(1)} \right\} \right] (1 - e^{-\beta_i^2 \bar{t}}). \tag{4.12}$$

Such an approximation immediately reduces the $(N + 1)$ -variable problem into a system with two variables only: $h^{(1)}$ and $\alpha_0^{(1)}$.

The approximate solution in (4.12) is then included into the integral mass conservation relation (4.8) which after rearrangements yields

$$\alpha_0^{(1)} = A(\bar{t}) \frac{dh^{(1)}}{d\bar{t}} + B(\bar{t})h^{(1)} - C(\bar{t}). \tag{4.13}$$

Here, $A(\bar{t})$, $B(\bar{t})$, $C(\bar{t})$ are temporal functions dependent on the zeroth-order quantities:

$$\left. \begin{aligned} A(\bar{t}) &= \frac{1 + \frac{2}{h^{(0)}} \sum_{i \neq 0} \frac{\eta_i^2 \dot{h}^{(0)}}{\beta_i^2} (1 - e^{-\beta_i^2 \bar{t}})}{\eta_0 + \frac{2}{h^{(0)}} \sum_{i \neq 0} \frac{\eta_i^2 \alpha_0^{(0)}}{\beta_i^2} (1 - e^{-\beta_i^2 \bar{t}})}, \\ B(\bar{t}) &= \frac{\sum_{i \neq 0} \frac{\eta_i^2}{[h^{(0)}]^2 \beta_i^2} (1 - e^{-\beta_i^2 \bar{t}})}{\eta_0 + \frac{2}{h^{(0)}} \sum_{i \neq 0} \frac{\eta_i^2 \alpha_0^{(0)}}{\beta_i^2} (1 - e^{-\beta_i^2 \bar{t}})}, \\ \text{and } C(\bar{t}) &= \frac{\sum_{i \neq 0} \eta_i \frac{d\alpha_i^{(0)}}{d\bar{t}} (1 - e^{-\beta_i^2 \bar{t}})}{\eta_0 + \frac{2}{h^{(0)}} \sum_{i \neq 0} \frac{\eta_i^2 \alpha_0^{(0)}}{\beta_i^2} (1 - e^{-\beta_i^2 \bar{t}})}. \end{aligned} \right\} \tag{4.14}$$

One can explicitly compute $A(\bar{t})$, $B(\bar{t})$, $C(\bar{t})$ from the known transient variation of $h^{(0)}$ and $\alpha_i^{(0)}$.

Finally, the simplified momentum relation (4.11) is considered for $i = 0$ and $\alpha_0^{(1)}$ is replaced by using (4.13). As a result, we derive the following linear second-order equation involving only one dependent variable $h^{(1)}$

$$\frac{d^2 h^{(1)}}{d\bar{t}^2} + G(\bar{t}) \frac{dh^{(1)}}{d\bar{t}} + H(\bar{t})h^{(1)} = F(\bar{t}). \tag{4.15}$$

Here, $G(\bar{t})$, $H(\bar{t})$, $F(\bar{t})$ are three time-dependent functions representing transient damping, restoring and forcing terms, respectively. These are numerically computed from their respective expressions

$$\left. \begin{aligned} G(\bar{t}) &= \frac{2\eta_0}{A(\bar{t})} \frac{\dot{h}^{(0)}}{h^{(0)}} + \frac{\dot{A}(\bar{t})}{A(\bar{t})} + \frac{B(\bar{t})}{A(\bar{t})} + \beta_0^2 - \frac{2\eta_0 \alpha_0^{(0)}}{h^{(0)}}, \\ H(\bar{t}) &= \frac{\eta_0}{A(\bar{t})[h^{(0)}]^2} + \frac{\dot{B}(\bar{t})}{A(\bar{t})} + \frac{B(\bar{t})}{A(\bar{t})} \left[\beta_0^2 - \frac{2\eta_0 \alpha_0^{(0)}}{h^{(0)}} \right], \\ \text{and } F(\bar{t}) &= \frac{\beta_0^2}{A(\bar{t})} \frac{d\alpha_0^{(0)}}{d\bar{t}} + \frac{\dot{C}(\bar{t})}{A(\bar{t})} + \frac{C(\bar{t})}{A(\bar{t})} \left[\beta_0^2 - \frac{2\eta_0 \alpha_0^{(0)}}{h^{(0)}} \right]. \end{aligned} \right\} \tag{4.16}$$

We present $G(\bar{t})$, $H(\bar{t})$, $F(\bar{t})$, for different geometries and initial conditions in figure 4.

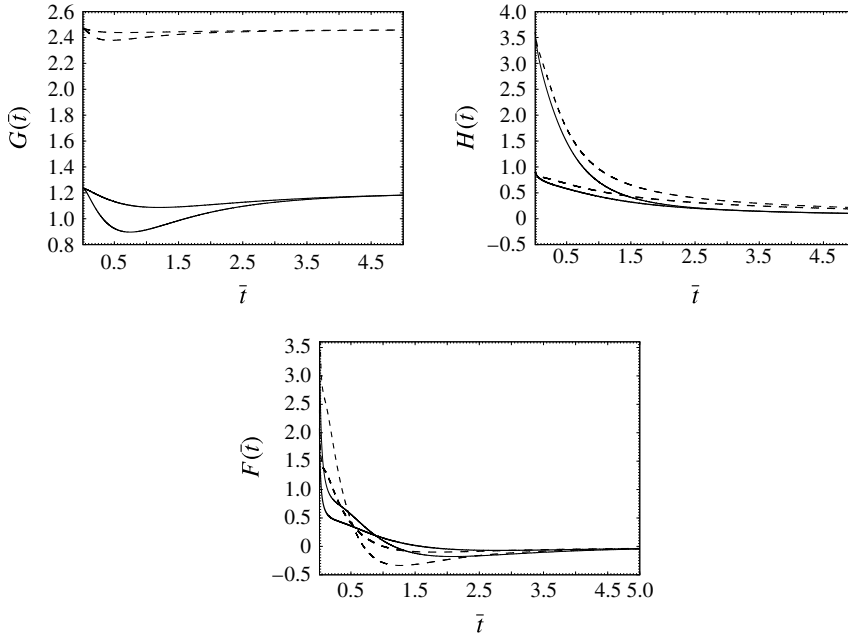


FIGURE 4. The quantities defined in (4.16) are plotted as functions of time \bar{t} for square channels (solid lines) and slit pores (dashed lines) with $\bar{h}_0 = 1.0$ (thick lines) and $\bar{h}_0 = 0.5$ (thin lines).

In figure 4, the effective dissipation in the system is represented by the function G . This is essentially the ratio between the damping factor and the mass, both of which increase proportionally with the intruded length. So G is expected to be approximately a constant in time. This is evident in figure 4.

In contrast, the function H manifests a restoring spring term due to the viscoelasticity of the liquid. For a gradual deceleration over a long time, the elastic effect in the medium becomes irrelevant. This happens because for time scales much larger than the duration of viscoelastic relaxation, the medium acts like a purely viscous fluid. So the restoration function H should monotonically decay to 0, as revealed in figure 4.

The crucial impact of viscoelasticity is captured by the forcing term F which underlines the discrepancy in stress due to the memory effect. The main contribution in F comes from the leading-order flow acceleration represented by the temporal derivative of $\alpha_i^{(0)}$. For a purely viscous system, the fluid first accelerates from rest under the action of the surface tension. Then, after some time, the flow starts to decelerate due to enhanced resistance coming from the increased length of the penetrated column. Accordingly, we expect F to change sign after an initial period of positive value. This is precisely what can be seen in figure 4. Such a reversal is the core reason explaining the oscillatory behaviour in figure 2.

4.4. Comparative studies between reduced mathematical models and exact simulations

We compute the leading-order deviation in the transport rate for a purely viscous case due to the viscoelastic effect in three independent ways. Firstly, we consider a very small Weissenberg number ($Wi = 0.01$) and solve (2.23) and (2.24) directly, as described in § 3. As a result, the departure between the results for mildly viscoelastic

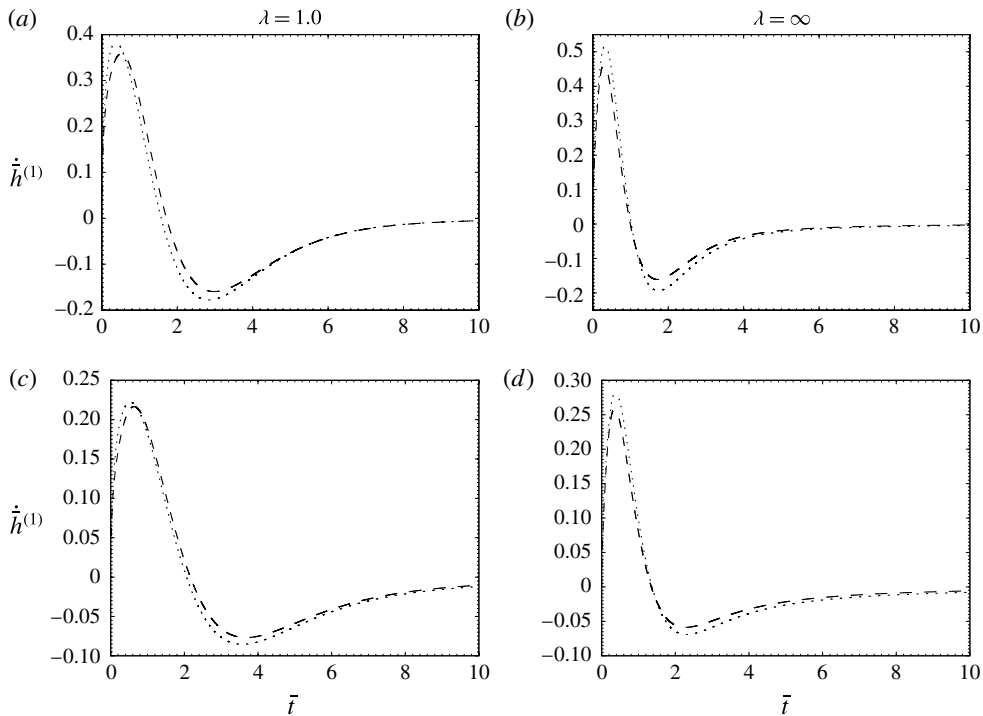


FIGURE 5. First-order deviation in penetration rate due to the viscoelastic effect is obtained as a function of time in three different ways for a square channel (*a,c*) and slit pore (*b,d*) where \bar{h}_0 is 0.5 (*a,b*) and 1.0 (*c,d*). We first use an approximate reduced description in (4.15) (dashed lines), and then the perturbative relations (4.8) and (4.10) (dotted lines). Also, the same results are directly computed from the departure between mildly viscoelastic ($Wi=0.01$) and purely viscous ($Wi=0$) systems using (2.23) and (2.24) (solid dots).

and purely viscous systems is calculated exactly so that first-order correction $\dot{h}^{(1)}$ in the transport rate can be obtained by dividing the difference by Wi . Then, $\dot{h}^{(1)}$ is also evaluated by solving the perturbation relation given by (4.8) and (4.10) using a Runge–Kutta method assuming a start-up problem from rest. Thirdly and finally, the approximate formulation given by (4.15) is exploited in another Runge–Kutta scheme to determine $\dot{h}^{(1)}$.

The three sets of simulations describing $\dot{h}^{(1)}$ as a temporal function are presented in figure 5 for a comparative study. We consider two different geometries and two separate initial conditions in figure 5. All cases show that the direct simulation and the exact perturbation corroborate each other precisely. It also reveals that the approximate model given by (4.15) predicts values which are very close to the other two results. Thus, we can assert the correctness of our numerical simulation and the validity of both the perturbative theory as well as the approximate reduced model.

The validity of the reduced model allows us to use its simplicity for an intuitive explanation of the oscillating temporal behaviour seen in both figures 2 and 5. The cause of the oscillation can be attributed to the fluctuating forcing function $F(\bar{t})$ given in figure 4 and defined in (4.15)–(4.16). A positive F makes $\dot{h}^{(1)} > 0$ at the initial time. However, the subsequent reversal in F induces an eventual reversal in $\dot{h}^{(1)}$ too. However, the latter happens after a certain delay which can be justified

by considering the phase difference due to the inertial second-order term and the restorative zeroth-order term in (4.15). The lag is also understandable from the causality perspective.

The dynamics of the system seems to be overdamped, as $\dot{h}^{(1)}$ approaches 0 gradually in the long-time limit. The reason for this is obvious from the functions in figure 4. The restorative term $H(\bar{t})$, representing the elastic effect in (4.15), decays with time whereas the dissipative term G remains more or less constant. This means that the system has to correspond to an overdamped situation for a large temporal scale.

5. Asymptotic analysis for the long-time dynamics

The exact simulation, the Weissenberg number perturbation and the reduced model show that the transport rate slows down over time. When the elapsed time is much larger than t_s , defined in (2.9), the motion inside the system is expected to decrease due to enhanced dissipation in the longer fluid column. In this section, we formulate an asymptotic theory to describe this decaying feature.

The analysis especially reveals how the long-time dynamics is modified by the viscoelastic effect. One can conclude intuitively that the impact of viscoelasticity should be reduced over time. Our asymptotic theory investigates the validity of this assumption, as well as estimates any subdominant contribution of the memory effect.

5.1. Rescaling of variables and perturbation expansion

The perturbation analysis considers a transport time scale t_o which is much larger than t_s , defined in (2.9). If time is normalized by t_o , the corresponding non-dimensional variable is defined as \tilde{t} . The rescaled time is related to \bar{t} by the following renormalization:

$$\tilde{t} = \epsilon \bar{t}, \tag{5.1}$$

where the ratio between t_s and t_o is ϵ which is identified as a small quantity based on which the perturbation theory is formulated.

We also take into account the corresponding rescaling of the intruded length and the amplitudes of the eigenfunctions. Accordingly, it is assumed that the leading orders of the viscous dissipation and the capillary force balance each other. Consequently, the rescaled penetration length and the n spectral amplitudes are respectively defined as

$$\tilde{h} = \sqrt{\epsilon} \bar{h}, \tag{5.2}$$

and

$$\tilde{\alpha}_n = \alpha_n / \sqrt{\epsilon}. \tag{5.3}$$

As pressure gradient due to surface tension is inversely proportional to penetration, the factor $\sqrt{\epsilon}$ has to be involved in the renormalized quantities in (5.2) and (5.3).

Then we use the following expansions in ϵ to identify the decay features in the dynamics

$$\tilde{h}(\tilde{t}) = \tilde{h}^{(0)}(\tilde{t}) + \epsilon \tilde{h}^{(1)}(\tilde{t}) + \dots, \tag{5.4}$$

and

$$\tilde{\alpha}_{nm}(\tilde{t}) = \tilde{\alpha}_{nm}^{(0)}(\tilde{t}) + \epsilon \tilde{\alpha}_{nm}^{(1)}(\tilde{t}) + \dots, \tag{5.5}$$

where the i th-order quantities in the small parameter ϵ are $\tilde{h}^{(i)}$ and $\tilde{\alpha}_{nm}^{(i)}$, respectively. The relation between $\tilde{h}^{(i)}$ and the corresponding i th-order decaying feature in \bar{h} is represented by the following transformation

$$\bar{h}^{(i)}(\bar{t}) = \epsilon^{i-(1/2)} \tilde{h}^{(i)}(\epsilon \bar{t}). \tag{5.6}$$

If the i th-order solutions are calculated properly, the transformation in (5.6) should ensure that the i th-order decay in \bar{h} is independent of ϵ . This invariance is a feature which can be used as a verification for the mathematical treatment.

Finally, the integral operator in (4.5) is recast in an expansion of ϵ after modifying the expression in terms of the transformed variables

$$\hat{L}_t \alpha_{nm}|_{\bar{i}} = \sum_{k=0}^{\infty} (-1)^k W_i^k \frac{M_k}{k!} \frac{d^k \alpha_{nm}}{d\bar{t}^k} \Big|_{\bar{i}} = \sqrt{\epsilon} \sum_{k=0}^{\infty} \epsilon^k (-1)^k W_i^k \frac{M_k}{k!} \frac{d^k \tilde{\alpha}_{nm}}{d\bar{t}^k} \Big|_{\bar{i}}. \tag{5.7}$$

Expansions of \hat{L}_t as well as the transformed quantities are substituted into (2.23) and (2.24) to obtain a series of relations corresponding to specific orders of ϵ . The leading-order and the next-order equations are the focus of the subsequent analysis.

5.2. The leading-order behaviour

The leading-order momentum equation in ϵ provides a simple algebraic relation

$$\tilde{\alpha}_{nm}^{(0)} = \frac{\eta_{nm}}{M_0 \beta_{nm}^2} \frac{1}{\tilde{h}^{(0)}} = \frac{\eta_{nm}}{\beta_{nm}^2} \frac{1}{\tilde{h}^{(0)}}, \tag{5.8}$$

where we recall $M_0 = 1$. When this relation is used in the leading-order mass conservation equation, a simple differential equation for $\tilde{h}^{(0)}$ can be derived

$$\frac{d\tilde{h}^{(0)}}{d\tilde{t}} = \sum_{n,m} \frac{\eta_{nm}^2}{\beta_{nm}^2} \frac{1}{\tilde{h}^{(0)}} = \frac{1}{\bar{k}} \frac{1}{\tilde{h}^{(0)}}. \tag{5.9}$$

Here, \bar{k} is a constant dependent on the cross-sectional geometry

$$\bar{k} = \frac{1}{\sum_{n,m} [\eta_{nm}^2 / \beta_{nm}^2]}, \tag{5.10}$$

which represents the cumulative viscous dissipation in the system.

The solution for (5.9) is

$$\tilde{h}^{(0)} = \sqrt{\frac{2\tilde{t}}{\bar{k}} + \tilde{c}_0^2}. \tag{5.11}$$

Consequently, the transformation in (5.6) gives the leading-order trend in \bar{h}

$$\bar{h}^{(0)} = \sqrt{\frac{2\bar{t}}{\bar{k}} + \bar{c}_0^2}, \tag{5.12}$$

as well as the long-time penetration rate

$$\dot{\bar{h}}^{(0)} = \frac{1}{\bar{k}\bar{h}^{(0)}} = \frac{1}{\sqrt{2\bar{k}\bar{t} + \bar{k}^2\bar{c}_0^2}}. \tag{5.13}$$

Here, \tilde{c}_0 and \bar{c}_0 are two integration constants which are related to the short-time dynamics and are irrelevant in the leading-order asymptotic feature

$$\lim_{\tilde{t} \rightarrow \infty} \bar{h}^{(0)} \approx \sqrt{\frac{2\tilde{t}}{k}} \tag{5.14}$$

and

$$\lim_{\tilde{t} \rightarrow \infty} \dot{\bar{h}}^{(0)} \approx \frac{1}{\sqrt{2k\tilde{t}}}. \tag{5.15}$$

It is to be noted that $\bar{h}^{(0)}$ and $\dot{\bar{h}}^{(0)}$ are independent of ϵ , confirming validity of the analysis.

It is evident that the leading-order decay does not involve the Weissenberg number Wi , as it is the same result also given by Washburn for a purely viscous fluid (Washburn 1921). This means that this asymptotic behaviour is not affected by viscoelasticity. Such an observation can be intuitively justified by the fact that a viscoelastic liquid acts as a purely viscous one in gradual transport under a long-time limit much greater than the relaxation time τ_v .

5.3. First-order correction in the decay characteristic

The effect of viscoelasticity on the long-time dynamics is manifested in the next-order correction in ϵ , as the corresponding term in the expansion of the memory integral involves Wi in (5.7). To highlight this fact, we obtain the solutions for $\tilde{\alpha}_{nm}^{(1)}$ and $\tilde{h}^{(1)}$.

Accordingly, the next-order momentum equation in ϵ is isolated

$$\tilde{\alpha}_{nm}^{(1)} = \left[\frac{-W_i M_1}{M_0^3 \bar{k}} \frac{\eta_{nm}}{\beta_{nm}^2} + \frac{1}{M_0^3 \bar{k}} \frac{\eta_{nm}}{\beta_{nm}^4} + \frac{(k' - 1/\bar{k}^2)}{M_0^3} \frac{\eta_{nm}}{\beta_{nm}^2} \right] \left(\frac{1}{\tilde{h}^{(0)}} \right)^3 - \frac{1}{M_0} \frac{\eta_{nm}}{\beta_{nm}^2} \frac{\tilde{h}^{(1)}}{[\tilde{h}^{(0)}]^2}, \tag{5.16}$$

where k' is a constant dependent on the cross-sectional geometry

$$k' = \sum_{n,m} \frac{\eta_{nm}^2}{\beta_{nm}^4}. \tag{5.17}$$

We substitute (5.16) in the mass conservation of similar order to derive the governing equation for $\tilde{h}^{(1)}$

$$\frac{d\tilde{h}^{(1)}}{d\tilde{t}} = \left(2\frac{k'}{\bar{k}} - \frac{W_i}{\bar{k}^2} - \frac{1}{\bar{k}^3} \right) \left(\frac{1}{\tilde{h}^{(0)}} \right)^3 - \frac{\tilde{h}^{(1)}}{[\tilde{h}^{(0)}]^2}, \tag{5.18}$$

where M_0 and M_1 are replaced by unity, as per (2.3).

We transform (5.18) into a convenient form by using (5.9)

$$\frac{d[\tilde{h}^{(1)}\tilde{h}^{(0)}]}{d\tilde{h}^{(0)}} = \left(2k' - \frac{W_i}{\bar{k}} - \frac{1}{\bar{k}^2} \right) \frac{1}{\tilde{h}^{(0)}}. \tag{5.19}$$

Finally, the solution for $\tilde{h}^{(1)}$ is obtained as

$$\tilde{h}^{(1)} = k_p \frac{[\ln(\tilde{h}^{(0)}/\tilde{c}_1^e)]}{\tilde{h}^{(0)}}, \tag{5.20}$$

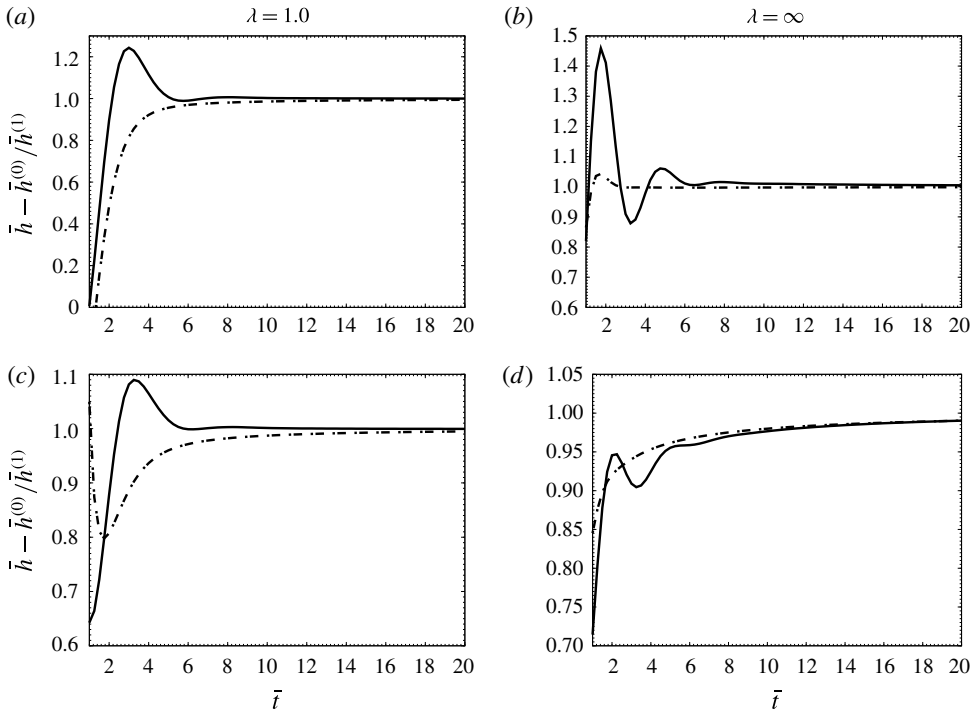


FIGURE 6. Difference between the actual intruded length and the leading-order asymptotic behaviour in (5.14) normalized by the corresponding first-order decay function in (5.22). The ratio is plotted as a function of the non-dimensional time for a square channel (a,c) and slit pore (b,d), where the prefilled length is 0.5 (a,b) and 1.0 (c,d). For each plot, the Weissenberg number is 0.5 (solid line) or 0.2 (dashed line).

where \tilde{c}_1^e is a integration constant dependent on the short-time dynamics and k_p is a factor defined below

$$k_p = 2k' - \frac{W_i}{k} - \frac{1}{k^2}. \tag{5.21}$$

Thus, the long-time decaying feature of $\bar{h}^{(1)}$ is given by the following ϵ -invariant expression

$$\lim_{\bar{t} \rightarrow \infty} \bar{h}^{(1)} \approx \frac{k_p}{\sqrt{2\bar{t}/k}} \left[\ln \left(\sqrt{\frac{\bar{t}}{k_1^e}} \right) \right], \tag{5.22}$$

where k_1^e is a constant related to \tilde{c}_1^e .

For mutual corroboration of the simulation and the asymptotic theory, we subtract the leading-order behaviour in (5.14) from the computed values of $\bar{h}^{(0)}$ obtained from the direct simulation. The difference is then divided by the first-order solution given in (5.22). The resulting ratio is plotted as a function of time \bar{t} in figure 6 for slit pores and square channels with different values of prefilled length h_0 and Weissenberg number Wi . All curves saturate to 1 in the long-time limit. This feature provides mutual corroboration between the computational data and the perturbation theory.

The higher-order perturbation analysis also shows how viscoelasticity affects the subdominant components of the asymptotic decay. This effect is represented by the factor k_p which is dependent on both the cross-sectional geometry and the

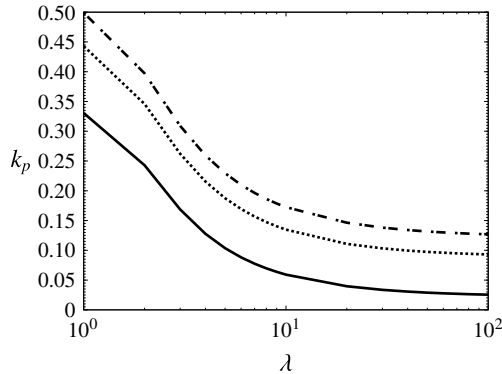


FIGURE 7. The geometry-dependent constant k_p defined in (5.21) is plotted as a function of the aspect ratio λ for $Wi=0.4$ (solid line), $Wi=0.2$ (dotted line) and $Wi=0.1$ (dash-dot line).

viscoelastic condition. This is why Weissenberg number appears in the expression of k_p in addition to its variation with geometric parameters.

In figure 7, we present the constant k_p as a function of the aspect ratio λ . We consider three values of Wi to show how k_p shifts with viscoelastic condition. For a slit pore, under the limit $Wi \rightarrow 0$, k_p should be $7/45$ which is matched by the computed result.

6. Summary and conclusion

In this article, we compute the time-dependent penetration length and intrusion rate of a mildly viscoelastic medium driven by surface tension inside a narrow capillary channel. To this end, eigenfunction expansion of the instantaneous velocity profile is used to derive a system of integro-differential equations. These coupled equations are solved simultaneously to determine the involved dependent variables which include the infiltrated distance and the unsteady eigen amplitudes.

We solve the coupled integro-differential equations with a fourth-order Runge–Kutta method assuming a start-up problem where an initially static prefilled column is driven from rest. The solution scheme ultimately produces the penetration distance and the intrusion rate as functions of time for a square channel and a slit pore. The simulation considers cases with varying prefilled length.

The temporal variation in the intrusion rate essentially reveals the effect of viscoelasticity on the infiltration dynamics. The fluid initially accelerates from rest under the capillary action. The normalized non-dimensional value of this initial acceleration is higher for stronger viscoelasticity because a stronger and more protracted memory implies a less resistive stress at the beginning of the motion. This is why initially the flow moves faster for higher Weissenberg number. After complete viscoelastic relaxation, however, the enhanced velocity induces increased resistance, prompting a significant retardation. As a result, we observe an overcompensation leading to an oscillatory feature in the time versus imbibition rate plots. Eventually, for all systems, the transport rate slows down asymptotically, as the longer fluid column creates more dissipation in the long-time limit. One expects that the leading-order temporal decay should not depend on the memory effect because all viscoelastic fluids act as a purely viscous fluid under on a long time scale. The computational findings justify this intuitive fact.

The short- and long-time behaviours of the system are further analysed by two respective perturbation theories. The first of these is based on a Weissenberg number expansion, which provides an insightful explanation for the oscillatory features in the intrusion rate and the ultimate decay in the dynamics. In contrast, the second one verifies the independence of the leading-order long-time variation in the viscoelasticity and quantifies how the next-order asymptotic characteristics can be affected by the memory effect.

The Weissenberg number perturbation is focused on the first two terms in the expansion of the variables. The leading order in Wi predicts the dynamics for a purely viscous fluid, whereas the next order shows the departure created by the viscoelasticity. We calculate this viscoelastic deviation in three ways. Firstly, it is computed directly by comparing the intrusion of a purely viscous fluid and the same for a system with very small Wi . Then, the difference due to the memory effect is also evaluated by solving the relation provided by rigorous perturbative analysis. Thirdly and finally, we propose a reduced model, where we have to solve a linear second-order inhomogeneous differential equation to find the correction in the intrusion rates. The results from all three methods corroborate each other with the expected accuracy. This validates our general simulation, perturbation theory and reduced model.

The second-order equation of the reduced model involves time-dependent damping, restoring and forcing terms. The temporal variations in these three quantities explain the oscillation and decay in the transport rate. The forcing term includes the contribution from the leading-order acceleration which reverses after an initial positive value. Such reversal causes the oscillating pattern in the time versus intrusion rate plots. Also, it is seen that the restorative spring constant in the equation decays to zero under the long-time limit while the dissipation remains more or less constant. Hence, the system has to be overdamped under the long-time limit, corroborating the asymptotic decay in the transport.

Our second perturbation analysis renders more a quantitative perspective on the asymptotic behaviour of the system under the long-time limit. It recovers Washburn's result for a purely viscous fluid (Washburn 1921) where the infiltrated length varies as the square root of time, irrespective of the viscoelastic condition represented by Wi . The memory effect influences the next-order decay, however, where the quantity varies inversely proportional to the square root of time. The corresponding proportionality constant has a linear dependence on Wi .

In the future, we will apply the presented theory to form the working principle of a rheometric device. The instrument will record the time versus penetration data from which the rheological properties of the medium can be predicted. For detection purposes, the theoretical prediction for the short- and long-time dynamics will be matched to the stored results by iterative selection of the effective viscoelastic scale τ_v . If the measurement is detailed enough, the memory function M can also be constructed in a similar iteration scheme in Fourier space.

Acknowledgement

This work is supported by NSF grant CBET-1034461.

REFERENCES

- ARADA, N., PIRES, M. & SEQUEIRA, A. 2005 Numerical simulation of shear-thinning Oldroyd-B fluid in curved pipes. *IASME Trans.* **2**, 948–959.

- AZESE, M. N. 2011 Modified time dependent penetration length and inlet pressure field in rectangular and cylindrical channel flows driven by non mechanical forces. *Trans. ASME J. Fluids Engng* **133**, 1112051.
- BAZILEVSKY, A. V., KORNEV, K. G., ROZHKOVA, A. N. & NEIMARK, A. V. 2003 Spontaneous absorption of viscous and viscoelastic fluids by capillaries and porous substrates. *J. Colloid Interface Sci.* **262**, 16–24.
- BHATTACHARYA, S., AZESE, M. N. & SINGHA, S. 2016 Rigorous theory for transient capillary imbibition in channels of arbitrary cross-section. *Theor. Comput. Fluid Dyn.* **31** (2), 137–157.
- BHATTACHARYA, S. & GURUNG, D. 2010 Derivation of governing equation describing time-dependent penetration length in channel flows driven by non-mechanical forces. *Anal. Chim. Acta* **666**, 51–54.
- CHEBBI, R. 2007 Dynamics of liquid penetration into capillary tubes. *J. Colloid Interface Sci.* **315**, 255–260.
- DAS, S., WAGHMARE, P. R. & MITRA, S. K. 2012 Early regimes of capillary filling. *Phys. Rev. E* **86**, 067301.
- FAN, Y., TANNER, R. & PHAN-TIEN, N. 2001 Fully developed viscous and viscoelastic flow in curved pipes. *J. Fluid Mech.* **440**, 327–357.
- FELDERHOF, B. U. 2009 Estimating the viscoelastic moduli of a complex fluid from observation of Brownian motion. *J. Chem. Phys.* **131**, 164904.
- GROISMAN, A., ENZELBERGER, M. & QUAKE, S. R. 2003 Microfluidic memory and control devices. *Science* **300**, 955–958.
- ICHIKAWA, N., HOSOKAWA, K. & MAEDA, R. 2004 Interface motion of capillary driven flow in rectangular microchannel. *J. Colloid Interface Sci.* **280**, 155–164.
- KANG, Y. J. & LEE, S. J. 2013 Blood viscoelasticity measurement using steady and transient flow controls of blood in a microfluidic analogue of Wheastone-bridge channe. *Biomicrofluidics* **7**, 054122.
- KHUZHAYOROV, B., AURIAULT, J. L. & ROYER, P. 2000 Derivation of macroscopic filtration law for transient linear viscoelastic fluid flow in porous medium. *Intl J. Engng Sci.* **38**, 487–505.
- KOSER, A. E. & PAN, L. C. 2013 Measuring material relaxation and creep recovery in a microfluidic device. *Lab on a Chip* **13**, 1850–1853.
- MARMUR, A. & COHEN, R. D. 1997 Characterization of porous media by the kinetics of liquid penetration: the vertical capillaries model. *J. Colloid Interface Sci.* **189**, 299–304.
- MITSOULIS, E. & HENG, F. L. 1987 Extrudate swell of Newtonian fluids from converging and diverging annular dies. *Rheol. Acta* **26**, 414–417.
- MORA, S. & MANNA, M. 2010 Saffman–Taylor instability of viscoelastic fluids from viscous fingering to elastic fracture. *Phys. Rev. E* **81**, 026305.
- PATANKAR, S. 1980 *Numerical Heat Transfer and Fluid Flow*. McGraw-Hill.
- QUERE, D. 1997 Inertial capillarity. *Eur. Phys. Lett.* **39**, 533–538.
- ROUSSE, P. E. JR. 1953 A theory of the linear viscoelastic properties of dilute solutions of coiling polymers. *J. Chem. Phys.* **21**, 1272–1280.
- STANGE, M., DREYER, M. E. & RATH, H. J. 2003 Capillary driven flow in circular cylindrical tubes. *Phys. Fluids* **15**, 2587–2601.
- SZEKELY, J., NEUMANN, A. W. & CHUANG, Y. K. 1970 the rate of capillary penetration and the applicability of the Washburn equation. *J. Colloid Interface Sci.* **35**, 273–278.
- WAGHMARE, P. & MITRA, S. 2010a On the derivation of pressure field distribution at the entrance of a rectangular channel. *Trans. ASME J. Fluids Engng* **132**, 054502.
- WAGHMARE, P. R. & MITRA, S. K. 2010b Modeling of combined electroosmotic and capillary flow in microchannels. *Anal. Chim. Acta* **663**, 117–126.
- WASHBURN, E. W. 1921 The dynamics of capillary flow. *Phys. Rev.* **17**, 273–283.
- ZHMUD, B. V., TIBERG, F. & HALLSTENSSON, K. 2000 Dynamics of capillary rise. *J. Colloid Interface Sci.* **228**, 263–269.
- ZILZ, J., SCHAFFER, C., WAGNER, C., POOLE, R. J., ALVES, M. A. & LINDER, A. 2014 Serpentine channels: micro-rheometers for fluid relaxation times. *Lab on a Chip* **14**, 351–358.